A fast radiative transfer model for visible through shortwave infrared spectral reflectances in clear and cloudy atmospheres

Chenxi Wang [a],*, Ping Yang [a], Shaima L. Nasiri [a], Steven Platnick [b], Bryan A. Baum [c], Andrew K. Heidinger [d], Xu Liu [e]

[a] Department of Atmospheric Sciences, Texas A&M University, College Station, TX 77843, USA
[b] Earth Sciences Division, NASA Goddard Space Flight Center, Greenbelt, MD 20771, USA
[c] Space Science and Engineering Center, University of Wisconsin-Madison, Madison, WI 53706, USA
[d] NOAA/NESDIS Center for Satellite Applications and Research, Madison, WI 53706, USA
[e] Science Directorate, NASA Langley Research Center, Hampton, VA 23681, USA

ARTICLE INFO

ABSTRACT

A computationally efficient radiative transfer model (RTM) for calculating visible (VIS) through shortwave infrared (SWIR) reflectances is developed for use in satellite and airborne cloud property retrievals. The full radiative transfer equation (RTE) for combinations of cloud, aerosol, and molecular layers is solved approximately by using six independent RTEs that assume the plane-parallel approximation along with a single-scattering approximation for Rayleigh scattering. Each of the six RTEs can be solved analytically if the bidirectional reflectance/transmittance distribution functions (BRDF/BTDF) of the cloud/aerosol layers are known. The adding/doubling (AD) algorithm is employed to account for overlapped cloud/aerosol layers and non-Lambertian surfaces. Two approaches are used to mitigate the significant computational burden of the AD algorithm. First, the BRDF and BTDF of single cloud/aerosol layers are pre-computed using the discrete ordinates radiative transfer program (DISORT) implemented with 128 streams, and second, the required integral in the AD algorithm is numerically implemented on a twisted icosahedral mesh. A concise surface BRDF simulator associated with the MODIS land surface product (MCD43) is merged into a fast RTM to accurately account for non-isotropic surface reflectance. The resulting fast RTM is evaluated with respect to its computational accuracy and efficiency. The simulation bias between DISORT and the fast RTM is large (e.g., relative error $> 5\%$) only when both the solar zenith angle (SZA) and the viewing zenith angle (VZA) are large (i.e., SZA $> 45°$ and VZA $> 70°$). For general situations, i.e., cloud/aerosol layers above a non-Lambertian surface, the fast RTM calculation rate is faster than that of the 128-stream DISORT by approximately two orders of magnitude.

1. Introduction

Fast forward radiative transfer models (RTMs) implemented for specific satellite-based instruments, also known as radiance simulators, are important to the radiance assimilation used in numerical weather prediction (NWP) systems [1–4] and in the operational retrievals of atmospheric profiles [5–7] as well as cloud [8–12] and aerosol [13] properties. While numerous studies focused on the fast radiance calculations in the infrared (IR) region ($\lambda > 4 \, \mu m$) [3,5,9–12,14,15], the forward radiance simulations in the IR spectral region are relatively straightforward compared with

* Corresponding author. Tel.: +1 979 845 5123.
  E-mail address: chenx.wang@geos.tamu.edu (C. Wang).

those in the visible through shortwave infrared (VIS/SWIR) regimes (0.4 μm < λ < 2.5 μm). For example, the sources of IR radiances, including thermal emission from the surface, atmosphere, cloud, and aerosol layers, do not show significant angular dependence, and the limited impact of the anisotropic feature of surface reflection can be ignored due to the small albedo [16,17]. Additionally, both cloud and aerosol particles absorb more energy in the IR spectral region [18–22] than in the VIS/SWIR spectral region mitigating relatively complicated scattering effects. In the VIS/SWIR region, however, the "quasi-isotropic" feature of radiance vanishes because of multiple scattering processes within the cloud/aerosol layers and with non-Lambertian surface reflection. Furthermore, the primary radiation source within the VIS/SWIR spectral region is solar radiation, giving rise to an azimuthal angular dependence of the radiance that is caused partially by the quasi-collimated direct solar beam. Consideration of both gaseous absorption and Rayleigh scattering effects makes the implementation of numerical simulation more difficult. If the cloud or aerosol layer is opaque, several of the well-known RTMs [23–27], which deal with the multiple scattering in the cloud and aerosol layers and reflective non-Lambertian surfaces require significant computational effort to simulate the radiance.

A number of challenges exist in the accurate forward simulation of non-clear sky top of the atmosphere (TOA) radiance in the VIS/NIR spectral region. First, the forward radiance simulator requires information about the cloud/aerosol layer, such as geometric height/thickness and optical/microphysical properties, and the atmospheric state, including the temperature, pressure, and humidity profiles. Modern satellite operational products and their corresponding algorithms use a variety of approaches to infer cloud and aerosol layer geometries [28–31], ambient temperature, pressure, and humidity [32,33]. A number of reanalysis products, such as the National Centers for Environmental Prediction/Global Data Assimilation System (NCEP/GDAS; [34]) and the NASA Global Modeling and Assimilation Office/Modern Era Retrospective-analysis for Research and Applications (GMAO/MERRA; [35]), provide near real-time meteorological data that facilitate the forward simulation.

Second, the bidirectional reflectance distribution function (BRDF) of a non-Lambertian surface is needed. The Moderate Resolution Imaging Spectroradiometer (MODIS) operational land surface product (MCD43) provides a series of parameters associated with a forward BRDF model [36,37] to reveal the directional variance of surface reflectance [38,39]. The surface BRDF over the ocean, largely determined by the surface wind speed [40], can also be simulated. The BRDF models for both ocean and land surfaces are well developed and have been validated using satellite-based and in-situ measurements [41]. However, the Lambertian surface assumption is still widely used in current satellite-based cloud retrieval algorithms, such as the ones for MODIS Collection 5 [42], the Spinning Enhanced Visible and Infrared Imager (SEVIRI), and the Advanced Very High Resolution Radiometer (AVHRR) [43].

Although many rigorous radiative transfer schemes, such as the adding–doubling (AD) algorithm [26,27] and the discrete ordinates radiative transfer (DISORT) method

[23], have been developed, they require substantial computational effort and are impractical for global satellite remote sensing applications. Thus, it is critical to develop computationally efficient RTM capabilities. In this paper, a computationally stable and efficient AD algorithm is explored that is designed to solve approximately the problem of radiation transfer in scattering and absorbing media (thermal emission is omitted for simplification) above an arbitrary non-Lambertian surface. Two novel features of this algorithm are in its treatment of Rayleigh scattering and an arbitrary number of cloud/aerosol layers and the associated solid angle integration.

To consider separately both the impact of Rayleigh scattering and the cloud/aerosol layers, we divided the full radiative transfer equation (RTE) into six independent sub-equations [44,45]. The total effect of multiple cloud/aerosol layers is solved numerically using the AD algorithm. The AD algorithm is known to be accompanied by a time consuming integration process over a conjunct solid angle associated with the two adjacent scattering and absorptive layers with the resulting integral known as "star products" [46,47]. One traditional solution is to calculate numerically the integral with a constant zenith–azimuth (select constant values for zenith and azimuth angles) discretization scheme [48]. The use of this discretization scheme in a fast RTM is inappropriate for two reasons. First, the radiance simulations slow down computationally in the zenith (or nadir) direction, i.e., the zenith angle cosine is near 1 (or −1), where the variation of BRDF is not significant. Second, the discrete solid angles in the region where the zenith angle cosine is near zero (i.e., "equator region") are larger than those in the zenith/nadir region with the regular discretization scheme. However, the BRDF always contains obvious variations in the "equator region", and, as a result, the numerical integration can lose significant accuracy. While we note that some AD codes have chosen to circumvent this loss of accuracy by using a constant cosine of zenith angle discretization (i.e., equal solid angle [26]), we have instead selected a twisted icosahedral grid [49] to calculate the integral efficiently.

The remainder of this paper is organized with the Atmosphere–Cloud/Aerosol–Surface system described in Section 2; the analytical solutions of the independent RTEs briefly presented in Section 3; the numerical approach for reducing the computational burden is introduced in Section 4; and, the validation and summary are discussed in Sections 5 and 6, respectively.

2. Scheme of the model

To take advantage of the well-accepted AD technique, the RTE solver is designed for a plane-parallel and vertically inhomogeneous medium above a reflective lower boundary. Specifically, the background consists of two clear layers without cloud or aerosol particles, and a "non-clear" layer containing multiple consecutive cloud or aerosol layers (Fig. 1), each of which is assumed to contain a homogeneous absorbing and/or scattering medium such that the spectral single-scattering albedo and phase functions are constant. The Rayleigh scattering between any two consecutive cloud/aerosol layers is neglected for simplicity. The extinction caused by the clear-sky layer between the surface and the
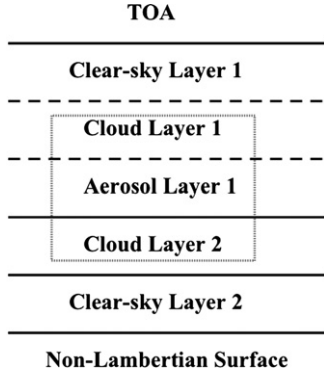
TOA

Clear-sky Layer 1

- - - - - - - - - - - - - - - -

Cloud Layer 1

- - - - - - - - - - - - - - - -

Aerosol Layer 1

Cloud Layer 2

Clear-sky Layer 2

Non-Lambertian Surface

Fig. 1. Illustrative diagram of a plane-parallel atmosphere consisting of two clear layers, multiple cloud/aerosol layers, and a non-Lambertian surface.

lowermost cloud/aerosol layer must be considered due to the non-negligible effects of water vapor and other gases. The sea-level Rayleigh optical thickness is generally smaller than 0.1 [50] in the spectral regions (0.55, 0.66, 0.87, and beyond 1.0 μm) primarily used to study surface, cloud, and aerosol properties. Consequently, the Rayleigh scattering can be accounted for based on a single-scattering approximation [45], meaning that only one scattering event between a single photon and an air molecule is assumed for all the clear layers in the column. A weakness of this approximation can be found for some cases, such as a high cirrus cloud over a low water cloud layer. Further study is required to efficiently take into account the Rayleigh scattering between consecutive non-clear layers.

Following the derivation of principles of invariance [44] and the Rayleigh scattering correction technique [45], we separate the complicated process into six independent events (Fig. 2). Photons are: (a) backward scattered by gas molecules within the upper clear layer; (b) first scattered by the upper clear layer and then reflected by the non-clear layer; (c) reflected by the non-clear layer and then scattered back toward the viewing direction by gas molecules; (d) directly reflected by the non-clear layer; (e) scattered by the lower gas molecules; and, (f) reflected due to the Rayleigh scattering occurring in the lower layer and then diffusely transmitted to the non-clear layer. The satellite-observed TOA bidirectional reflectance (R_{TOA}) contributed by the six events can be expressed as the summation of the six individual parts.

3. Analytical solution

To specify the geometry of the incident solar beam and the viewing direction, the TOA radiance contributed by each of the six independent parts can be derived by solving six individual RTEs with different boundary conditions and can be expressed in terms of bidirectional reflectance functions. The definition of bidirectional reflectance is in the form:

$$R(\mu_v, \varphi_v, -\mu_i, \varphi_i) = \frac{\pi I(0, \mu_v, \varphi_v)}{\mu_i F_0}, \tag{1}$$

where μ is the cosine of zenith angle, φ is the azimuth angle, F_0 is the incident solar irradiance at the TOA, and

the subscripts i and v indicate the incident and viewing directions respectively. The spectral dependence is implied. The six bidirectional reflectance functions can be expressed as follows:

$$R_I = \frac{\omega_u P_{-iv}}{4(\mu_i + \mu_v)} \left[1 - \exp\left(\frac{-\tau_u(\mu_i + \mu_v)}{\mu_i \mu_v}\right) \right], \tag{2a}$$

$$R_{II} = \frac{\omega_u}{4\pi} \exp\left(-\frac{\tau_u}{\mu_v}\right) \int_0^{2\pi} \int_0^1 \frac{\mu'}{\mu' - \mu_i} P_{ij} R_{jv} \left[\exp\left(\frac{-\tau_u}{\mu'}\right) - \exp\left(\frac{-\tau_u}{\mu_i}\right) \right] d\mu' d\varphi', \tag{2b}$$

$$R_{III} = \frac{\omega_u}{4\pi\mu_v} \exp\left(-\frac{\tau_u}{\mu_i}\right) \int_0^{2\pi} \int_0^1 \frac{\mu' \mu_v}{\mu' - \mu_v} R_{ij} P_{jv}$$
$$\left[\exp\left(\frac{-\tau_u}{\mu'}\right) - \exp\left(\frac{-\tau_u}{\mu_v}\right) \right] d\mu' d\varphi', \tag{2c}$$

$$R_{IV} = \exp\left(-\frac{\tau_u}{\mu_i}\right) \exp\left(-\frac{\tau_u}{\mu_v}\right) R_{iv}, \tag{2d}$$

$$R_V = \frac{\omega_l P_{-iv}}{4(\mu_i + \mu_v)} \exp\left[-\frac{\mu_i + \mu_v}{\mu_i \mu_v}(\tau_c + \tau_u)\right] \left[1 - \exp\left(-\frac{\mu_i + \mu_v}{\mu_i \mu_v}\tau_l\right)\right], \tag{2e}$$

$$R_{VI} = \frac{\omega_l}{4\pi} \exp\left(-\frac{\tau_c + \tau_u}{\mu_i}\right) \exp\left(-\frac{\tau_u}{\mu_v}\right) \int_0^{2\pi} \int_0^1 \frac{\mu'}{\mu_i + \mu'} P_{-ij} T_{jv} d\mu' d\varphi', \tag{2f}$$

where the subscript j is associated with μ' and φ'; τ_u, τ_l, and τ_c correspond to the extinction optical thickness of the upper clear layer, lower clear layer, and the total effect of non-clear layer (i.e., consisting of consecutive cloud/aerosol layers), respectively; and ω_u and ω_l are the single-scattering albedo values of the upper and lower clear layers respectively. Under the assumption that energy is conserved during the Rayleigh scattering process, the single-scattering albedo of a clear layer can be expressed as

$$\omega = \frac{\tau_R}{\tau_R + \tau_a}, \tag{3}$$

where τ_R and τ_a indicate the Rayleigh and absorption optical thicknesses respectively. Consequently, the denominator of Eq. (3) is essentially the extinction optical thickness of a clear layer, while P, R, and T, respectively, represent the Rayleigh phase function, the bidirectional reflectance, and transmittance (diffuse) function of the non-clear layer. The two subscripts associated with each of P, R, T functions specify the incoming direction (the former) and the outgoing direction (the latter). Additionally, a negative sign before the two subscripts of P indicates that the signs of the incoming and outgoing zenith angle cosines are different.

The BRDF of a cloud (or aerosol)–surface system (R_{cs}) or cloud–cloud (or aerosol) system (R_{cc}) and the bidirectional transmittance distribution function (BTDF) of a cloud–cloud (T_{cc}) system are necessary to derive Eqs. (2b)–(2f). In the rigorous AD algorithm [26,27], the R and T functions of a single layer cloud/aerosol are numerically computed with the so-called doubling process. This process starts with a cloud/aerosol layer with an infinitesimal optical thickness (e.g., $\tau \sim 10^{-8}$ in numerical calculation) so that the single-scattering approximation can be applied. However, it is time-consuming if the cloud/aerosol layer is not optically thin. In this study, the computational burden resulting from
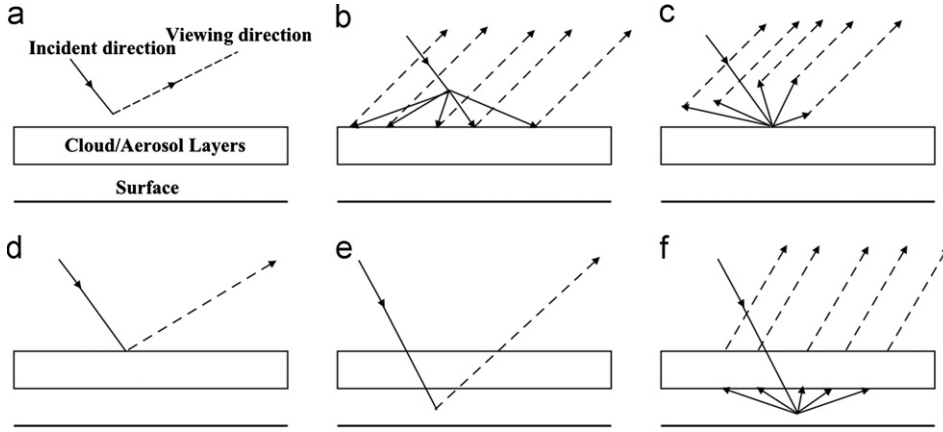
Fig. 2. Six possible paths of photons transferred within the atmosphere–cloud/aerosol system. Photons are: (a) backward scattered by air molecules of the upper clear layer; (b) forward scattered by the upper clear layer and then reflected by the non-clear layer; (c) reflected by the non-clear layer and then scattered back toward the viewing direction due to the Rayleigh scattering; (d) directly reflected by the non-clear layer; (e) scattered by the air molecules within the lower layer (no interaction with the non-clear layer); and, (f) reflected due to the Rayleigh scattering occurring in the lower layer and then diffusely transmitted to the non-clear layer. The dashed lines indicate the reflected radiation in the direction of satellite-based instrument.
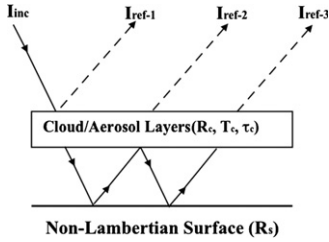

Fig. 3. Illustrative diagram of the adding algorithm applied to the cloud/aerosol and non-Lambertian surface system.

the doubling process is alleviated by using a set of pre-computed R and T lookup tables (LUTs) for single homogeneous cloud or aerosol layers [15]. The AD method (although the doubling process is avoided, we will continue to use the AD term for convention) is employed to simulate R and T functions of the non-clear layer and the reflective non-Lambertian surface.

The cloud–surface system is illustrated in Fig. 3. As mentioned in Section 2, the absorptive gases within the clear layer between the surface and cloud lower boundary need to be taken into account. The first-order Rayleigh scattering has been included in the fifth and sixth independent events (shown in Fig. 2e and f). As shown in Fig. 3, the optical thicknesses of the non-clear layer and clear layer are τ_c and τ_a, while R_c and T_c indicate the BRDF and BTDF of the non-clear layer. The nth order of radiance reflected by the cloud–surface system is I_{ref-n}. The total reflected intensity, I_{ref}, is expressed as the summation of all the orders. If we define a star product operator [46] as

$$X(\mu,\varphi)*Y(\mu,\varphi) = \frac{1}{\pi}\int_0^{2\pi}\int_0^1 X(\mu,\varphi)Y(\mu,\varphi)\mu d\mu d\varphi, \quad (4)$$

where X and Y are two arbitrary functions of μ and φ then the first three orders of intensity are given by:

$$I_{ref-1} = I_{inc,i}*R_{iv}, \quad (5a)$$

$$I_{ref-2} = I_{inc,i}*(T_{c,ij}+\delta_{ij}t_{c,j})*t_{a,j}R_{s,jk}t_{a,k}*(T_{c,kv}+\delta_{kv}t_{c,v}), \quad (5b)$$

$$I_{ref-3} = I_{inc,i}*(T_{c,ij}+\delta_{ij}t_{c,j})*t_{a,j}R_{s,jk}t_{a,k}*R_{c,kl}t_{a,l}*R_{s,lm}$$
$$t_{a,m}*(T_{c,mv}+\delta_{mv}t_{c,v}), \quad (5c)$$

where the subscripts i, j, k, l, m, and v indicate the direction of incident or reflected (transmitted) radiance. For example, $T_{c,ij}$ indicates the BTDF for a situation in which the incident radiance toward direction i is scattered by the cloud/aerosol particles and eventually transmitted out of the layer toward direction j. $I_{inc,i}$ is the incident radiance toward the directions, i, $t_{c,j}$, and $t_{a,j}$, and defined as follows:

$$t_{c,j} = \exp\left(-\frac{\tau_c}{\mu_j}\right), \quad (6a)$$

$$t_{a,j} = \exp\left(-\frac{\tau_a}{\mu_j}\right), \quad (6b)$$

which are the direct transmittance functions of the non-clear and clear layers. δ_{ij} is the Kronecker delta defined as

$$\delta_{ij} = \begin{cases} 1, & i=j \\ 0, & i\neq j \end{cases}. \quad (7)$$

with the definition of bidirectional reflectance, Eq. (1), $R_{cs,iv}$ can be given by:

$$R_{cs,iv} = R_{c,iv}+(T_{c,ij}+\delta_{ij}t_{c,j})*U_{cs,jp}*(T_{c,pv}+\delta_{pv}t_{c,v}), \quad (8)$$

where $U_{cs,jp}$ is defined as

$$U_{cs,jp} = t_{a,j}R_{s,jp}t_{a,p} + t_{a,j}R_{s,jk}t_{a,k}*R_{c,kl}t_{a,l}*R_{s,lp}t_{a,p}$$
$$+ t_{a,j}R_{s,jk}t_{a,k}*R_{c,kl}t_{a,l}*R_{s,lm}t_{a,m}*R_{c,mn}t_{a,n}*R_{s,np}t_{a,p} + \cdots. \quad (9)$$

The cloud–cloud system is essentially the same as the cloud–surface combination. In a like manner, $R_{cc,iv}$ and $T_{cc,iv}$ can be expressed as

$$R_{cc,iv} = R_{1,iv}+(T_{1,ik}+\delta_{ik}t_{1,k})*U_{cc,kp}*(T_{1,pv}+\delta_{pv}t_{1,v}), \quad (10)$$

$$T_{cc,ij} = T_{1,ik} * t_{a,k} T_{2,kj} + T_{1,ij} t_{a,j} t_{2,j} + t_{1,i} t_{a,i} T_{2,ij}$$
$$+ (T_{1,ik} + \delta_{ik} t_{1,k}) * D_{cc,kq} * (T_{2,qj} + \delta_{qj} t_{2,j}), \tag{11}$$

and $U_{cc,kp}$ and $D_{cc,kq}$ are defined as

$$U_{cc,kp} = t_{a,k} R_{2,kp} t_{a,p} + t_{a,k} R_{2,kl} t_{a,l} * R_{1,lm} t_{a,m} * R_{2,mp} t_{a,p}$$
$$+ t_{a,k} R_{2,kl} t_{a,l} * R_{1,lm} t_{a,m} * R_{2,mn} t_{a,n} * R_{1,no} t_{a,o} * R_{2,op} t_{a,p} + \cdots, \tag{12}$$

$$D_{cc,kq} = t_{a,k} R_{2,kl} t_{a,l} * R_{1,lq} t_{a,q} + t_{a,k} R_{2,kl} t_{a,l} * R_{1,lm} t_{a,m} *$$
$$R_{2,mn} t_{a,n} * R_{1,nq} t_{a,q}$$
$$+ t_{a,k} R_{2,kl} t_{a,l} * R_{1,lm} t_{a,m} * R_{2,mn} t_{a,n} * R_{1,no} t_{a,o} * R_{2,op} t_{a,p} *$$
$$R_{1,pq} t_{a,q} + \cdots, \tag{13}$$

where the subscripts 1 and 2 indicate the upper and lower cloud/aerosol layers. Note that t_a indicates the transmittance function between the two non-clear layers.

4. Numerical solution

In the previous section, we derived a generally applicable solution of the TOA bidirectional reflection. However, to achieve a rapid and accurate model for operational applications, we need an appropriate way to select the quadrature points and weights of the spherical solid angle integration shown in Eq. (4). With a simple discretization scheme, the integral could be easily calculated on a grid with constant zenith angle and azimuth angle intervals [48]. However, several problems arise associated with a regular zenith–azimuth discretization scheme. For example, the area of differential element rapidly decreases towards the zenith. As a result, the numerical integration based on this grid scheme increases the computational burden in the pole region (i.e., μ is close to 1), and decreases the accuracy near the equator (i.e., μ is close to 0).

Various studies have focused on the approaches of discretization on a sphere [51,52], and many of these methods have already been applied in numerical models [49]. In this study, we conduct the numerical calculation on a twisted icosahedral grid (Fig. 4), which has been successively utilized to numerically calculate the shallow-water equations in the atmospheric general circulation model (AGCM) [53] developed by Colorado State University. The primary advantages of a twisted icosahedral grid are (1) the elemental triangles have similar areas and shapes, which stabilizes the accuracy of the numerical integration; and, (2) the grid is symmetric with respect to the "equator" (i.e., none of the elemental triangles spans the "equator"), (3) this discretization scheme does not use a Fourier cosine series to factor out the azimuth dependence [23,54]. These features simplify the adding processes; however, one must be very careful in generating the BRDF/BTDF database of cloud/aerosol layers on a twisted icosahedral gird due to the significant forward peak of the particle phase function resulting from diffraction.

Many numerical methods [55,56] have been developed to mitigate the effect of the strong forward peak so that the phase function can be approximated as a summation of Legendre Polynomials with limited terms. However, the truncated phase functions (especially for large particles) in the forward directions (e.g., scattering angle $< 5°$) are larger than those in the semi-forward directions (e.g.,
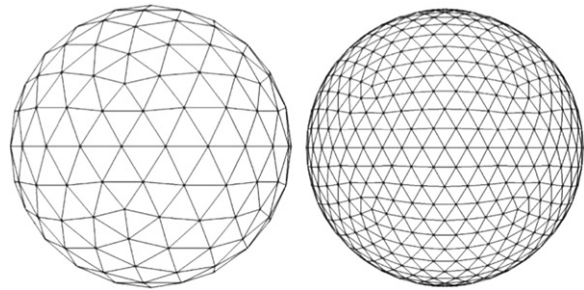

Fig. 4. Twisted icosahedrons inscribed in unit spherical surfaces. Left panel: 320 small triangles. Right panel: 1280 small triangles.
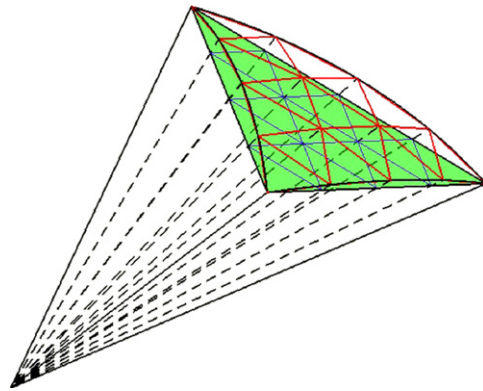

Fig. 5. An example of dividing a triangle into 16 small triangles, which are continually projected onto the spherical surface.

$5° <$ scattering angle $< 10°$) [56]. For this reason, in addition to using the delta-fit method [56] to truncate the phase function in the generation of both transmittance and reflectance LUTs, we continually refine the elemental triangles in the forward directions when calculating the diffuse transmittance LUTs. The use of icosahedral grid makes this step easy. Specifically, the triangles in the forward directions (i.e., scattering angle $< 5°$) are first divided into 16 or 64 sub-triangles with approximately the same area and then projected onto the spherical surface (see Fig. 5). The diffuse transmittance function in the forward direction is the average of the 16 or 64 transmittance functions calculated in the normal directions of the re-projected sub-triangles.

In accordance with the order of six independent events, we successively give their contributions to the TOA bidirectional reflectance in the form of numerical solutions. Assume that a twisted icosahedron has $2N$ elemental facets, half of which are located in the upward hemisphere. The area of the nth facet in the upward hemisphere is A_n. The surface area of the upward hemisphere is then given by:

$$S = \sum_{n=1}^{N} A_n. \tag{14}$$

The numerical forms of R_I to R_{VI} shown in Eq. (2) can be expressed as

$$R_I = \frac{\omega_u P_{-iv}}{4(\mu_i + \mu_v)}[1 - \exp(-c\tau_u)], \tag{15a}$$

$$R_{II} = \frac{\omega_u}{2S} t_{u,v} \left[\sum_{\substack{j=1 \\ \mu_j \neq \mu_i}}^{N} \left(\frac{\mu_j}{\mu_j - \mu_i} \right) P_{ij} R_{jv} A_j (t_{u,j} - t_{u,i}) + \lim_{\mu_j \to \mu_i} \left(\frac{\tau_u}{\mu_j} P_{ij} R_{jv} A_j t_{u,j} \right) \right], \tag{15b}$$

$$R_{III} = \frac{\omega_u}{2S\mu_v} t_{u,i} \left[\sum_{\substack{j=1 \\ \mu_j \neq \mu_v}}^{N} \left(\frac{\mu_j \mu_v}{\mu_j - \mu_v} \right) R_{ij} P_{jv} A_j (t_{u,j} - t_{u,v}) + \lim_{\mu_j \to \mu_v} \left(\tau_u P_{ij} R_{jv} A_j t_{u,j} \right) \right], \tag{15c}$$

$$R_{IV} = t_{u,i} t_{u,v} R_{iv}, \tag{15d}$$

$$R_V = \frac{\omega_l P_{-iv}}{4(\mu_i + \mu_v)} \exp[-c(\tau_c + \tau_u)][1 - \exp(-c\tau_l)], \tag{15e}$$

$$R_{VI} = \frac{\omega_l}{2S} t_{cu,i} t_{u,v} \sum_{j=1}^{N} \frac{\mu_j}{\mu_i + \mu_j} P_{-ji} T_{jv} A_j, \tag{15f}$$

where c is a coefficient defined as

$$c = \frac{\mu_i + \mu_v}{\mu_i \mu_v}, \tag{16}$$

and $t_{cu,i}$ is the direct transmittance function:

$$t_{cu,i} = \exp\left(-\frac{\tau_u + \tau_c}{\mu_i} \right). \tag{17}$$

The BRDF or BTDF of a cloud/aerosol layer or surface can be simply expressed in the form of $N \times N$ matrices, e.g., $\mathbf{R}_c$, $\mathbf{T}_c$, and $\mathbf{R}_s$. Hence, $R_{s,jk}$ shown in Eq. (5) represents the element at the jth row and kth column of matrix $\mathbf{R}_s$. Additionally, the star product can be rewritten as

$$X(\mu, \varphi) * Y(\mu, \varphi) = f \sum_{i=1}^{N} X_i Y_i \mu_i A_i, \tag{18}$$

where f is a normalization factor defined as

$$f = \frac{2}{\sum_{i=1}^{N} A_i} = \frac{2}{S}. \tag{19}$$

Through using matrix multiplication and Eq. (18), we conclude that the star product of two bidirectional reflectance matrices, e.g., $\mathbf{R}_c$ and $\mathbf{R}_s$, can be expressed as

$$\mathbf{R}_c * \mathbf{R}_s = f\overline{\mathbf{R}}_c \mathbf{R}_s. \tag{20}$$

The definition of the notation "bar" is

$$\overline{\mathbf{R}} = \begin{bmatrix} R_{11} A_1 \mu_1 & R_{12} A_2 \mu_2 & \cdots & R_{1N} A_N \mu_N \\ R_{21} A_1 \mu_1 & : & : & : \\ : & : & : & : \\ R_{N1} A_1 \mu_1 & \cdots & \cdots & R_{NN} A_N \mu_N \end{bmatrix}. \tag{21}$$

Therefore, $\mathbf{U}_{cs}$ in Eq. (9) can be expressed as

$$\mathbf{U}_{cs} = \mathbf{R}_{gsg} + f^2 \overline{\mathbf{R}}_{gsg} \mathbf{V}_{cs} + f^4 \overline{\mathbf{R}}_{gsg} (\overline{\mathbf{V}}_{cs} \mathbf{V}_{cs}) + \cdots, \tag{22}$$

$$\mathbf{V}_{cs} = \overline{\mathbf{R}}_{cg} \mathbf{R}_{sg}, \tag{23}$$

where the matrices $\mathbf{R}_{gsg}$, $\mathbf{R}_{cg}$, and $\mathbf{R}_{sg}$ are defined as follows:

$$\mathbf{R}_{gsg} = \begin{bmatrix} t_{a,1} R_{s,11} t_{a,1} & t_{a,1} R_{s,12} t_{a,2} & \cdots & t_{a,1} R_{s,1N} t_{a,N} \\ t_{a,2} R_{s,21} t_{a,1} & : & : & : \\ : & : & : & : \\ t_{a,N} R_{s,N1} t_{a,1} & \cdots & \cdots & t_{a,N} R_{s,NN} t_{a,N} \end{bmatrix}, \tag{24a}$$

$$\mathbf{R}_{cg} = \begin{bmatrix} R_{c,11} t_{a,1} & R_{c,12} t_{a,2} & \cdots & R_{c,1N} t_{a,N} \\ R_{c,21} t_{a,1} & : & : & : \\ : & : & : & : \\ R_{c,N1} t_{a,1} & \cdots & \cdots & R_{c,NN} t_{a,N} \end{bmatrix}, \tag{24b}$$

$$\mathbf{R}_{sg} = \begin{bmatrix} R_{s,11} t_{a,1} & R_{s,12} t_{a,2} & \cdots & R_{s,1N} t_{a,N} \\ R_{s,21} t_{a,1} & : & : & : \\ : & : & : & : \\ R_{s,N1} t_{a,1} & \cdots & : & R_{s,NN} t_{a,N} \end{bmatrix}. \tag{24c}$$

Hence, based on Eq. (20), we can replace the formulation of the bidirectional reflectance of the cloud–surface system shown in Eq. (8) by the following equations:

$$\mathbf{R}_{cs} = \mathbf{R}_c + f^2 \overline{\mathbf{T}}_c \mathbf{W}_{cs} + f\mathbf{X}_{cs} + \mathbf{Y}_{cs}, \tag{25a}$$

$$\mathbf{W}_{cs} = \overline{\mathbf{U}}_{cs} \mathbf{T}_c, \tag{25b}$$

$$\mathbf{W}'_{cs} = \overline{\mathbf{T}}_c \mathbf{U}_{cs}. \tag{25c}$$

$\mathbf{X}_{cs}$ is a symmetric matrix whose entries can be generally expressed as

$$X_{cs,ij} = W_{cs,ij} t_{c,i} + W'_{cs,ij} t_{c,j}, \tag{25d}$$

and the general expression of entries of matrix $\mathbf{Y}_{cs}$ is

$$Y_{cs,ij} = t_{c,i} U_{cs,ij} t_{c,j}. \tag{25e}$$

Similarly, the bi-directional reflectance matrix $\mathbf{R}_{cc}$ for a cloud–cloud system is given by

$$\mathbf{R}_{cc} = \mathbf{R}_1 + f^2 \overline{\mathbf{T}}_1 \mathbf{W}_{cc} + f\mathbf{X}_{cc} + \mathbf{Y}_{cc}, \tag{26a}$$

where

$$\mathbf{W}_{cc} = \overline{\mathbf{U}}_{cc} \mathbf{T}_1, \tag{26b}$$

$$\mathbf{W}'_{cc} = \overline{\mathbf{T}}_1 \mathbf{U}_{cc}, \tag{26c}$$

$$X_{cc,ij} = W_{cc,ij} t_{1,i} + W'_{cc,ji} t_{1,j}, \tag{26d}$$

$$Y_{cc,ij} = t_{1,i} U_{cc,ij} t_{1,j}, \tag{26e}$$

$$\mathbf{U}_{cc} = \mathbf{R}_{g2g} + f^2 \overline{\mathbf{R}}_{g2g} \mathbf{V}_{cc} + f^4 \overline{\mathbf{R}}_{g2g} (\overline{\mathbf{V}}_{cc} \mathbf{V}_{cc}) + \cdots, \tag{26f}$$

$$\mathbf{V}_{cc} = \overline{\mathbf{R}}_{1g} \mathbf{R}_{2g}, \tag{26g}$$

and the corresponding bidirectional transmittance matrix $\mathbf{T}_{cc}$ is given by:

$$\mathbf{T}_{cc} = f^2 \overline{\mathbf{T}}_1 \mathbf{E}_{cc} + f(\overline{\mathbf{T}}_1 \mathbf{T}_2 + \mathbf{G}_{cc}) + \mathbf{H}_{cc}, \tag{27a}$$

where

$$\mathbf{E}_{cc} = \overline{\mathbf{D}}_{cc} \mathbf{T}_2, \tag{27b}$$

$$\mathbf{D}_{cc} = f\mathbf{V}'_{cc} + f^3 \overline{\mathbf{V}'_{cc}} \mathbf{V}'_{cc} + f^5 [\overline{\mathbf{V}'_{cc}} (\overline{\mathbf{V}'_{cc}} \mathbf{V}'_{cc})] + \cdots, \tag{27c}$$

$$\mathbf{V}'_{cc} = \overline{\mathbf{R}}_{g2g}\mathbf{R}_{1g}, \tag{27d}$$

$$G_{cc,ij} = E_{cc,ij}t_{1,i} + F_{cc,ij}t_{2,j}, \tag{27e}$$

$$\mathbf{F}_{cc} = \overline{\mathbf{T}}_1\mathbf{D}_{cc}, \tag{27f}$$

$$H_{cc,ij} = t_{1,i}D_{cc,ij}t_{2,j} + T_{1,ij}t_{a,j}t_{2,j} + t_{1,i}t_{a,i}T_{2,ij}. \tag{27g}$$

Note that the definitions of $\mathbf{R}_{1g}$, $\mathbf{R}_{2g}$, and $\mathbf{R}_{g2g}$ are similar to those $\mathbf{R}_{cg}$, $\mathbf{R}_{sg}$, and $\mathbf{R}_{gsg}$, shown in Eqs. (24a)–(24c). Generally, the entries in $\mathbf{U}_{cs}$, $\mathbf{U}_{cc}$, and $\mathbf{D}_{cc}$ rapidly converge if the first and second orders of reflected radiance are considered (i.e., consider the first two terms of the right-hand sides of Eqs. (9), (12) and (13)). A simple exponential interpolation method is used to calculate the BRDF of cloud–surface system at user defined viewing zenith angles (VZA).

5. Model validation

To validate, we implement a set of comparisons between the newly developed fast RTM and a benchmark model, DISORT run using 128 streams, with respect to both the model accuracy and computational efficiency. We compare the TOA reflectance simulations obtained by both models for two scenes: (1) a single ice cloud layer and (2) overlapped ice cloud layers. The ice cloud microphysical [57] and optical properties [58–60] employed in the comparison are the same as those used in the current operational MODIS Collection 5 algorithm. The precomputed ice cloud bidirectional reflectance database is generated on the twisted icosahedral grid with 320 elemental facets (i.e., $N=160$ in Eq. (14)). Fig. 6 shows the relative errors of the fast model simulated TOA BRDFs at 0.64 μm as functions of the VZA for the background, which includes a single ice cloud layer and a reflective non-Lambertian surface. The dependence of the relative error on the solar zenith angle (SZA) is demonstrated by using solid, dotted, and dashed lines to give the relative errors in small (10°), medium (35°), and large (50°) SZA situations.

In general, the fast model provides satisfactory simulations in the case of a single ice cloud layer located above a non-Lambertian surface. The relative errors are smaller than 1% if the SZA is smaller than 35°. Note that the relative errors of the optically thick (e.g., $\tau=5$, lower panel of Fig. 6) cloud layer cases are slightly smaller than those of the moderately thick (e.g., $\tau=2$, upper panel of Fig. 6) cloud layer cases. The BTDF of a thick cloud is smaller than the BTDF of a moderately thick cloud and the errors resulting from the numerical integration in the adding process may be mitigated. The relative errors are maximized if both the VZA and SZA are large (i.e., up to 6% if VZA > 70° and SZA > 45°), which may be caused by the relative large variation of cloud BRDF function in these satellite geometries. Future work, such as restructuring grids near the "equator region" to improve model accuracy for large VZA and SZA cases, is necessary.

The influence of multiple cloud layers on the accuracy of the model simulation is considered by simulating overlapped ice cloud layers above a non-Lambertian surface. Similarly,
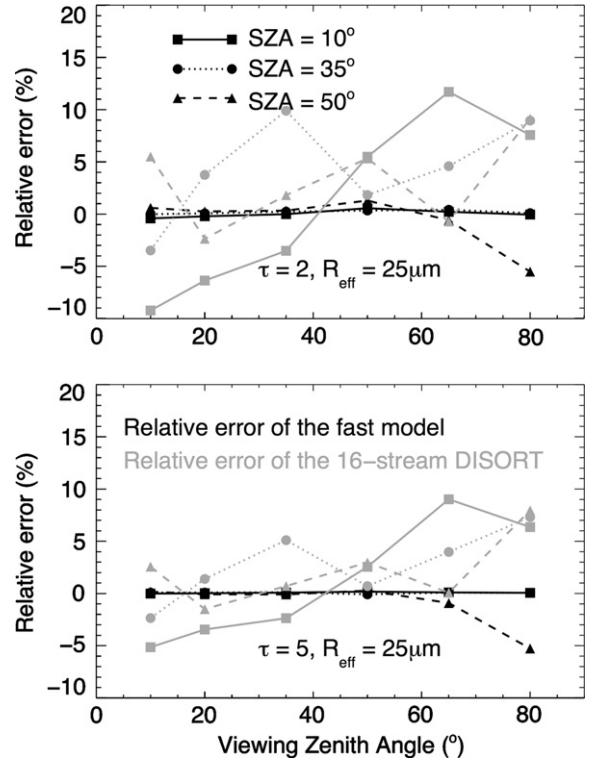

Fig. 6. Relative errors of TOA BRDFs at 0.64 μm simulated by the fast model (black) and the 16-stream DISORT (gray) in comparison with the benchmark model (i.e., DISORT with 128-stream). Single ice cloud layer and a non-Lambertian surface are considered. Three SVA values, 10°, 35°, and 50°, are employed and their corresponding results are demonstrated using solid lines, dotted lines, and dashed lines. Upper panel: $\tau=2.0$ (at 0.64 μm), effective radius (R_{eff})=25 μm; lower panel: $\tau=5.0$, $R_{eff}=25$ μm.

comparisons between DISORT and the fast model (see Fig. 7) indicate that the accuracy of the current fast model maintains an acceptable level even if the multiple cloud layers give rise to more complicated processes in the forward simulation. However, the relative errors exceed 1% when the SZA is large and the upper cloud layer is transparent. It is possible that the relatively large bias is caused by the average of upper layer BTDF in the forward directions (e.g., scattering angle < 5°) since the forward diffuse transmittance is maximized when the cloud is transparent.

With respect to the computational efficiency, a detailed comparison is demonstrated in Fig. 8. As expected, the computational efficiency of the current fast model is maximized for the case of a single cloud layer over a Lambertian surface. The BRDF and BTDF of a cloud/aerosol layer can be extracted easily from the pre-computed database and, more importantly, no additional adding procedure is required in the simulation based on the single-scattering approximation of clear-sky layers. When the presence of either a non-Lambertian surface or multiple cloud layers is taken into account, the efficiencies of both the DISORT and the fast model decrease, though by different magnitudes. The fast model calculates 80–90 times faster than the DISORT for the cases of two overlapped ice cloud layers above a reflective non-Lambertian surface. The computational efficiency of DISORT gradually decreases with an increase in
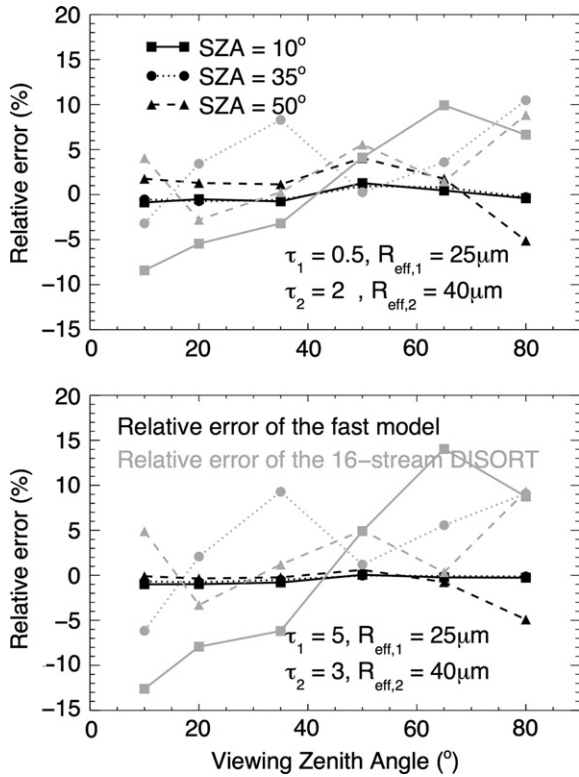
Fig. 7. Same as Fig. 6, but for the overlapped ice cloud layers + non-Lambertian surface cases. Upper panel: $\tau_1 = 0.5$, $\tau_2 = 2.0$, $R_{eff,1} = 25$ μm, $R_{eff,2} = 40$ μm; lower panel: $\tau_1 = 5.0$, $\tau_2 = 3.0$, $R_{eff,1} = 25$ μm, $R_{eff,2} = 40$ μm.
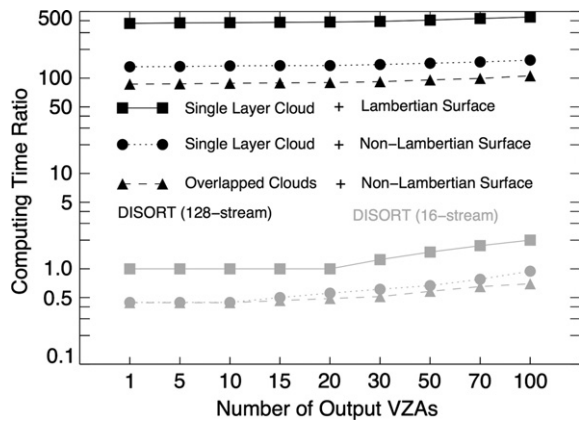

Fig. 8. The computing time ratio of DISORT (black: 128-stream mode; gray: 16-stream mode) to the fast model as a function of number of VZA. The ratio is independent to cloud optical and microphysical properties. Three scenes are considered: single layer cloud + Lambertion surface (solid line), single layer cloud + non-Lambertian surface (dotted line), and overlapped clouds + non-Lambertian surface (dashed line).

the number of user defined computing angles (i.e., not Gaussian quadrature angles) due to additional interpolation of computing angles to user defined VZA. However, the increase in number of output VZA does not significantly decrease the computational efficiency of the fast model primarily because the most time consuming process in the forward simulation is the numerical integration during the

adding processes. For current remote sensing purposes, such as pixel-level cloud retrieval and forward simulation coupled with a particular satellite-based instrument, the calculation is based on specified solar-satellite geometry, and for most cases, the result (i.e., TOA BRDF) at a unique VZA is required. However, for scientific research purposes, such as the study of model sensitivities to different factors, the model simulations on a series of VZAs and azimuthal angles may be desired. In these cases, this fast model has the advantage of computational efficiency. Specifically, the fast model runs 160 times, and 100 times faster than the DISORT for a single layer with overlapped cloud layers above a non-Lambertian surface.

DISORT results based on a 16-stream calculation are also employed for comparison, as shown in Figs. 6–8. Although the computing times of the fast model and the 16-stream DISORT have the same order of magnitude, as evident from Fig. 8, the relative errors of a 16-stream DISORT simulation can exceed 10% for several geometries (see Figs. 6 and 7).

6. Summary

This study focuses on the development of a fast and accurate RTM for cloud property retrieval purposes in the solar spectral region. To do this, we separate the complex radiation transfer process into six relatively simple events governed by six independent RTEs and particular boundary conditions such that analytical solutions can be obtained under the plane-parallel approximation. The AD algorithm is employed to calculate the total BRDF of the consecutive non-clear (i.e., cloud/aerosol) layers, as well as to consider the directional variation of surface reflectance. Two approaches are used in the fast RTM to increase the speed of the AD algorithm. First, the major time consuming process, the doubling process, is avoided by using pre-computed LUTs. Second, the twisted icosahedral discretization scheme is adopted to improve the efficiency and accuracy of the numerical integration.

The model is validated by comparison with the 128-stream DISORT. As demonstrated in Section 5, the performance of this fast RTM is satisfactory in terms of both computing efficiency and accuracy. To be more specific, this model is approximately 500 times faster than DISORT for the case of one cloud or aerosol layer above a Lambertian surface because of the use of pre-computed BRDF/BTDF LUTs. With either an increase of non-clear layers or the consideration of reflective non-Lambertian surfaces, the efficiency of both the fast RTM and DISORT decreases but by different magnitudes. However, the fast RTM still performs approximately 100 times faster than DISORT if two overlapped cloud layers and a non-Lambertian surface are considered. Additionally, the fast RTM exhibits a satisfactory simulation accuracy in the range of possible satellite–solar geometries. Indeed, the biases between the RTM and DISORT abruptly increase when both SZA and VZA angles exceed particular threshold values (i.e., SZA > 45° and VZA > 70°). For most instruments aboard a polar-orbiting satellite, the VZA values are generally smaller than 70°, such as MODIS (~65°) and the Visible/Infrared Imager Radiometer Suite

(VIIRS, $\sim 70°$). For this reason, this fast RTM can be applied to both forward modeling and cloud/aerosol retrieval and is suitable for various space-based or aircraft based observations in the VIS/NIR region.

Acknowledgments

References

[1] Weng FZ, Liu QH. Satellite data assimilation in numerical weather prediction models. Part I: forward radiative transfer and Jacobian modeling in cloudy atmospheres. J Atmos Sci 2003;60:2633–46.

[2] Weng FZ, Zhu T, Yan BH. Satellite data assimilation in numerical weather prediction models. Part II: uses of rain-affected radiances from microwave observations for hurricane vortex analysis. J Atmos Sci 2007;64:3910–25.

[3] Saunders R, Matricardi M, Brunel P. An improved fast radiative transfer model for assimilation of satellite radiance observations. Quart J Roy Meteorol Soc 1999;125:1407–25.

[4] Saunders R, Rayer P, Brunel P, von Engeln A, Bormann N, Strow L, et al. A comparison of radiative transfer models for simulating Atmospheric Infrared Sounder (AIRS) radiances. J Geophys Res-Atmos 2007;112:D01S90.

[5] Strow LL, Hannon SE, De Souza-Machado S, Motteler HE, Tobin D. An overview of the AIRS radiative transfer model. IEEE Trans Geosci Remote Sens 2003;41:303–13.

[6] Jin X, Li J. Improving moisture profile retrieval from broadband infrared radiances with an optimized first-guess scheme. Remote Sens Lett. 2010;1:231–8.

[7] Han Y. A rapid radiative transfer model for SSMIS UAS channels that takes the earth-rotation doppler shift and Zeeman effects into account. In: 11th specialist meeting on Microwave Radiometry and Remote Sensing of the Environment (MicroRad); 2010. p. 37–42.

[8] Huang HL, Yang P, Wei H, Baum BA, Hu YX, Antonelli P, et al. Inference of ice cloud properties from high spectral resolution infrared observations. IEEE Trans Geosci Remote Sens 2004;42:842–50.

[9] Wei H, Yang P, Li J, Baum BA, Huang HL, Platnick S, et al. Retrieval of semitransparent ice cloud optical thickness from atmospheric infrared sounder (AIRS) measurements. IEEE Trans Geosci Remote Sens 2004;42:2254–67.

[10] Dubuisson P, Giraud V, Chomette O, Chepfer H, Pelon J. Fast radiative transfer modeling for infrared imaging radiometry. J Quant Spectrosc Radiat Transfer 2005;95:201–20.

[11] Wang C, Yang P, Baum BA, Platnick S, Heidinger AK, Hu YX, et al. Retrieval of ice cloud optical thickness and effective particle size using a fast infrared radiative transfer model. J Appl Meteorol Climatol 2011;50:2283–97.

[12] Wang C, Yang P, Platnick S, Heidinger AK, Baum BA, Greenwald T, et al. Retrieval of ice cloud properties from AIRS observations based on a fast high-spectral resolution radiative transfer model. J Appl Meteorol Climatol, http://dx.doi.org/10.1175/JAMC-D-12-020.1, in press.

[13] Hsu NC, Si-Chee T, King MD, Herman JR. Deep Blue retrievals of Asian aerosol properties during ACE-Asia. IEEE Trans Geosci Remote Sens 2006;44:3180–95.

[14] Niu JG, Yang P, Huang HL, Davies JE, Li J, Baum BA, et al. A fast infrared radiative transfer model for overlapping clouds. J Quant Spectrosc Radiat Transfer 2007;103:447–59.

[15] Zhang Z, Yang P, Kattawar G, Huang H-L, Greenwald T, Li J, et al. A fast infrared radiative transfer model based on the adding–doubling method for hyperspectral remote-sensing applications. J Quant Spectrosc Radiat Transfer 2007;105:243–63.

[16] Wan ZM, Li ZL. A physics-based algorithm for retrieving land-surface emissivity and temperature from EOS/MODIS data. IEEE Trans Geosci Remote Sens 1997;35:980–96.

[17] Ruston B, Weng FZ, Yan BH. Use of a one-dimensional variational retrieval to diagnose estimates of infrared and microwave surface emissivity over land for ATOVS sounding instruments. IEEE Trans Geosci Remote Sens 2008;46:393–402.

[18] Hale GM, Querry MR. Optical constants of water in the 200-nm to 200-μm wavelength region. Appl Opt 1973;12:555–63.

[19] Warren SG, Brandt RE. Optical constants of ice from the ultraviolet to the microwave: a revised compilation. J Geophys Res 2008;113: D14220.

[20] Sokolik I, Andronova A, Johnson TC. Complex refractive index of atmospheric dust aerosols. Atmos Environ Pt A: Gen Top 1993;27: 2495–502.

[21] Volz FE. Infrared refractive index of atmospheric aerosol substances. Appl Opt 1972;11:755–9.

[22] Levoni C, Cervino M, Guzzi R, Torricella F. Atmospheric aerosol optical properties: a database of radiative characteristics for different components and classes. Appl Opt 1997;36:8031–41.

[23] Stamnes K, Tsay SC, Wiscombe W, Jayaweera K. Numerically stable algorithm for discrete-ordinate-method radiative transfer in multiple scattering and emitting layered media. Appl Opt 1988;27:2502–9.

[24] Collins DG, Blattner WG, Wells MB, Horak HG. Backward Monte Carlo calculations of the polarization characteristics of the radiation emerging from spherical-shell atmospheres. Appl Opt 1972;11: 2684–96.

[25] Plass GN, Kattawar GW. Monte Carlo calculations of light scattering from clouds. Appl Opt 1968;7:415–9.

[26] Twomey S, Jacobowitz H, Howell HB. Matrix methods for multiple-scattering problems. J Atmos Sci 1966;23:289–98.

[27] Hansen JE, Hovenier JW. The doubling method applied to multiple scattering of polarized light. J Quant Spectrosc Radiat Transfer 1971;11:809–12.

[28] Platnick S, King MD, Ackerman SA, Menzel WP, Baum BA, Riedi JC, et al. The MODIS cloud products: algorithms and examples from Terra. IEEE Trans Geosci Remote Sens 2003;41:459–73.

[29] Winker DM, Vaughan MA, Omar A, Hu YX, Powell KA, Liu ZY, et al. Overview of the CALIPSO mission and CALIOP data processing algorithms. J Atmos Oceanic Technol 2009;26:2310–23.

[30] Vaughan MA, Powell KA, Kuehn RE, Young SA, Winker DM, Hostetler CA, et al. Fully automated detection of cloud and aerosol layers in the CALIPSO lidar measurements. J Atmos Oceanic Technol 2009;26:2034–50.

[31] Menzel WP, Smith WL, Stewart TR. Improved cloud motion wind vector and altitude assignment using vas. J Clim Appl Meteorol 1983;22:377–84.

[32] Rodgers CD. Retrieval of atmospheric-temperature and composition from remote measurements of thermal-radiation. Rev Geophys 1976;14:609–24.

[33] Kuo CC, Staelin DH, Rosenkranz PW. Statistical iterative scheme for estimating atmospheric relative-humidity profiles. IEEE Trans Geosci Remote Sens 1994;32:254–60.

[34] Derber JC, Parrish DF, Lord SJ. The new global operational analysis system at the National Meteorological Center. Weather Forecast 1991;6:538–47.

[35] Rienecker MM, Suarez MJ, Todling R, Bacmeister J, Takacs L, Liu HC, et al. The GEOS-5 data assimilation system—documentation of Versions 5.0.1, 5.1.0, and 5.2.0. In: Technical report series on global modeling and data assimilation. NASA/TM; 2008. p. 27.

[36] Lucht W, Schaaf CB, Strahler AH. An algorithm for the retrieval of albedo from space using semiempirical BRDF models. IEEE Trans Geosci Remote Sens 2000;38:977–98.

[37] Schaaf CB, Gao F, Strahler AH, Lucht W, Li XW, Tsang T, et al. First operational BRDF, albedo nadir reflectance products from MODIS. Remote Sens Environ 2002;83:135–48.

[38] Ross JK. The radiation regime and architecture of plant stands. The Hague, Boston Hingham, Mass: Dr. W. Junk Publishers Distributed by Kluwer Boston; 1981.

[39] Li XW, Strahler AH. Geometric–optical bidirectional reflectance modeling of the discrete crown vegetation canopy—effect of crown shape and mutual shadowing. IEEE Trans Geosci Remote Sens 1992;30:276–92.

[40] Cox C, Munk W. Measurement of the roughness of the sea surface from photographs of the suns glitter. J Opt Soc Am 1954;44:838–50.

[41] Salomon JG, Schaaf CB, Strahler AH, Gao F, Jin YF. Validation of the MODIS Bidirectional Reflectance Distribution Function and Albedo retrievals using combined observations from the Aqua and Terra platforms. IEEE Trans Geosci Remote Sens 2006;44:1555–65.

[42] King MD, Tsay S-C, Platnick SE, Wang M, Liou K-N . Cloud retrieval algorithms for MODIS: optical thickness, effective particle radius and thermodynamic phase. MODIS Algorithm Theoretical Basis Document: NASA; 1997.

[43] Meirink JF, Roebelling R, Wolters E, Deneke H. In: Schulz J, editor. Algorithm theoretical basis document Cloud Physical Products AVHRR/SEVIRI. EUMETSAT; 2010.

[44] Ambartzumian VA. Theoretical astrophysics. New York: Pergamon Press; 1958.

[45] Wang MH, King MD. Correction of Rayleigh scattering effects in cloud optical thickness retrievals. J Geophys Res 1997;102: 25915–26.

[46] Liou K-N. An introduction to atmospheric radiation. 2nd ed. Amsterdam; Boston: Academic Press; 2002.

[47] Wendisch M, Yang P. Theory of atmospheric radiative transfer: a compresensive introduction. 1st ed. Weinheim, Germany: Wiley-VCH; 2012.

[48] Mobley CD. Light and water: radiative transfer in natural waters. San Diego: Academic Press; 1994.

[49] Heikes R, Randall DA. Numerical-integration of the shallow-water equations on a twisted icosahedral Grid.1. Basic design and results of tests. Mon Weather Rev 1995;123:1862–80.

[50] Bodhaine BA, Wood NB, Dutton EG, Slusser JR. On Rayleigh optical depth calculations. J Atmos Oceanic Technol 1999;16:1854–61.

[51] Stuhne GR, Peltier WR. New icosahedral grid-point discretizations of the shallow water equations on the sphere. J Comput Phys 1999;148:23–58.

[52] Górski KM, Hivon E, Banday AJ, Wandelt BD, Hansen FK, Reinecke M, et al. HEALPix: a framework for high-resolution discretization and fast analysis of data distributed on the sphere. Astrophys J 2005;622:759.

[53] Heikes R, Randall DA. Numerical-Integration of the shallow-water equations on a twisted icosahedral Grid.2. A detailed description of the grid and an analysis of numerical accuracy. Mon Weather Rev 1995;123:1881–7.

[54] Chandrasekhar S. Radiative transfer. New York: Dover Publications; 1960.

[55] Wiscombe WJ. Delta-M method—rapid yet accurate radiative flux calculations for strongly asymmetric phase functions. J Atmos Sci 1977;34:1408–22.

[56] Hu YX, Wielicki B, Lin B, Gibson G, Tsay SC, Stamnes K, et al. δ-Fit: a fast and accurate treatment of particle scattering phase functions with weighted singular-value decomposition least-squares fitting. J Quant Spectrosc Radiat Transfer 2000;65:681–90.

[57] Baum BA, Heymsfield AJ, Yang P, Bedka ST. Bulk scattering properties for the remote sensing of ice clouds. Part I: microphysical data and models. J Appl Meteorol 2005;44:1885–95.

[58] Baum BA, Yang P, Heymsfield AJ, Platnick S, King MD, Hu YX, et al. Bulk scattering properties for the remote sensing of ice clouds. Part II: narrowband models. J Appl Meteorol 2005;44:1896–911.

[59] Yang P, Liou KN, Wyser K, Mitchell D. Parameterization of the scattering and absorption properties of individual ice crystals. J Geophys Res 2000;105:4699–718.

[60] Zhang Z, Yang P, Kattawar GW, Tsay S-C, Baum BA, Hu Y, et al. Geometrical-optics solution to light scattering by droxtal ice crystals. Appl Opt 2004;43:2490–9.